

Strain-engineered Peierls instability in layered perovskite $\text{La}_3\text{Ni}_2\text{O}_7$ from first principlesYasuhide Mochizuki,¹ Hirofumi Akamatsu,^{1,2,*} Yu Kumagai,³ and Fumiyasu Oba^{1,3,4}¹Laboratory for Materials and Structures, Institute of Innovative Research, Tokyo Institute of Technology, Yokohama 226-8503, Japan²Department of Applied Chemistry, Kyushu University, 744 Motoooka, Fukuoka 819-0395, Japan³Materials Research Center for Element Strategy, Tokyo Institute of Technology, Yokohama 226-8503, Japan⁴Center for Materials Research by Information Integration, Research and Services Division of Materials Data and Integrated System, National Institute for Materials Science, Tsukuba 305-0047, Japan

(Received 30 November 2017; revised manuscript received 9 October 2018; published 7 December 2018)

Using first-principles calculations, we predict a strong coupling of lattice, charge, and spin degrees of freedom in Ruddlesden-Popper phase $\text{La}_3\text{Ni}_2\text{O}_7$, which enables a phase control with epitaxial strain. While the bulk ground state is metallic, moderate compressive strain is found to trigger a Peierls transition to an insulating state in concurrence with a breathing distortion of NiO_6 octahedra. The Peierls transition is microscopically interpreted as a band-gap opening arising from lifting and lowering of the Ni $d-e_g$ states due to the octahedral breathing.

DOI: [10.1103/PhysRevMaterials.2.125001](https://doi.org/10.1103/PhysRevMaterials.2.125001)

State-of-the-art thin-film growth techniques have been providing new avenues not only for the discovery of novel functional materials, but also for the exploration of structural phases with novel properties that cannot be accessed in bulk equilibrium states [1]. Without chemical substitution, epitaxial strain is able to tune coupled multiple degrees of freedom such as spin, charge, and lattice, and thereby breaks a delicate balance between two or more competing phases with distinct structural distortion, magnetic order, and electric conductivity. Perovskite-related transition-metal oxides are one of the most studied systems in terms of strain-engineered functionalities [2–5]. Their diverse electronic properties, including ferromagnetism, ferroelectricity, and superconductivity, are closely correlated with lattice distortions involving rotation, tilting, and deformation of the oxygen-coordinated octahedra enclosing the B -site cations because most of these properties originate from the d electrons of the B -site cations [6]. This leads to a lattice-charge-spin coupling, through which lattice distortions induced by epitaxial strain can give rise to drastic changes of the electronic, magnetic, and dielectric properties.

Ruddlesden-Popper double-layered perovskite $\text{La}_3\text{Ni}_2\text{O}_7$ has gotten plenty of attention because of the structural and electronic similarity to high- T_c superconducting cuprates [7–18]. Recently, a high-quality $\text{La}_3\text{Ni}_2\text{O}_7$ thin film has been successfully fabricated [19], which motivates the exploration of epitaxial strain-induced structural phases and properties. In this compound, the average formal charge of Ni ion is $+2.5$ ($d^{7.5}$). This material takes a low-spin configuration; the t_{2g} states are fully occupied by 6 electrons, and the remaining 1.5 electrons are occupied in the e_g states. The $(\text{LaNiO}_3)_2$ perovskite bilayers are separated by the LaO rocksalt layers [Fig. 1(a)], resulting in quasi-two-dimensional (quasi-2D) electric conductivity. Interestingly, the electric conductivity strongly depends on oxygen nonstoichiometry. Stoichiometric

$\text{La}_3\text{Ni}_2\text{O}_7$ is metallic down to low temperatures, while the oxygen deficiency leads to insulating behavior at room temperature and the resistivity is increased with an increase in oxygen vacancies [9–11,13,16]. Oxygen-excess $\text{La}_3\text{Ni}_2\text{O}_{7.05}$ exhibits a metal-insulator (MI) transition at 128 K [15]. In this context, stoichiometric $\text{La}_3\text{Ni}_2\text{O}_7$ is located near the MI phase boundary. The origin of nonstoichiometry-induced insulating nature still remains unclear. Charge and orbital ordering on the NiO_2 planes induced by oxygen vacancy ordering was attributed to the insulating states for oxygen-deficient $\text{La}_3\text{Ni}_2\text{O}_{7-\delta}$. On the other hand, the MI transition observed for oxygen-excess $\text{La}_3\text{Ni}_2\text{O}_{7+\delta}$ was suggested to result from freezing of charge-density wave (CDW) [12,15]. The detailed mechanism behind the charge ordering and the CDW condensation and the relevant lattice distortions, however, have not been clearly identified. In addition, applying quasihydrostatic pressure alters the MI transition temperatures with a rate of ~ -10 K/GPa for oxygen-excess $\text{La}_3\text{Ni}_2\text{O}_{7+\delta}$ [15,17]. This implies that epitaxial strain could also switch the borderline metal $\text{La}_3\text{Ni}_2\text{O}_7$ to an insulator.

In this paper, we report first-principles calculations exploring the ground-state crystal, electronic, and magnetic structures of pristine $\text{La}_3\text{Ni}_2\text{O}_7$ under epitaxial strain. We find that compressive strain drives an MI transition, and identify the relevant lattice distortion as breathing of NiO_6 octahedra [Fig. 1(b)]. We elucidate the underlying mechanism; a fine change of the electronic band structure by compressive strain triggers a Peierls transition concurrent with the lattice distortion and the change of spin configuration.

Our first-principles calculations were carried out using the projector-augmented-wave (PAW) method [20], the PBEsol generalized gradient approximation (GGA) functional [21], and a $+U$ correction as implemented in VASP [22,23]. The Dudarev formulation was adopted for the $+U$ correction [24]. We examined $U_{\text{eff}} = U - J = 0, 1.5, 3, 5, \text{ and } 7$ eV, where U and J are onsite Coulomb and exchange interaction. Note that we focus mainly on the results obtained using

*h.akamatsu@cstf.kyushu-u.ac.jp

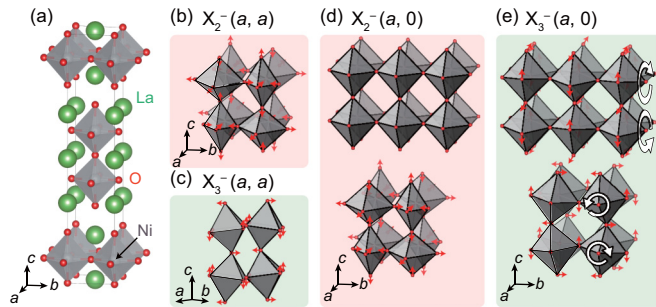


FIG. 1. (a) Distortion-free aristotype $I4/mmm$ structure of $\text{La}_3\text{Ni}_2\text{O}_7$. Solid lines indicate its conventional cell. Lattice distortion modes corresponding to breathing of the NiO_6 octahedra transforming like irreps (b) $X_2^-(a, a)$ and (d) $X_2^-(a, 0)$ and octahedral tilting transforming like irreps (c) $X_3^-(a, a)$ and (e) $X_3^-(a, 0)$. For simplicity, only relevant octahedra are shown.

$U_{\text{eff}} = 7$ eV. The results obtained with lower U_{eff} are illustrated in Sec. VIII of the Supplemental Material [25]. PAW data sets with radial cutoffs 1.5, 1.3, and 0.8 Å for La, Ni, and O, respectively, were used with a cutoff energy of 550 eV for plane waves. The following states were treated as valence electrons: $5s$, $5p$, $5d$, and $6s$ for La, $3d$ and $4s$ for Ni, and $2s$ and $2p$ for O. Lattice constants and internal coordinates were optimized until residual stress and forces converged down to 0.04 GPa and 10 meV/Å, respectively. Phonon frequencies were derived from the calculated force constants using PHONOPY [26]. We chose a $\sqrt{2} \times \sqrt{2} \times 1$ supercell of the $I4/mmm$ conventional cell for exploring stable structures so that the zone boundary special points $X(0, 0, \frac{1}{2})$ and $M(\frac{1}{2}, \frac{1}{2}, -\frac{1}{2})$ are folded into the $\Gamma(0,0,0)$ point (see details in the Supplemental Material, Sec. I [25]). We considered seven AFM configurations A1, A2, C1, C2, F2, G1, and G2 types, as well as an ferromagnetic (FM) configuration (F1 type) shown in Fig. S2 of the Supplemental Material [25], which cover the interbilayer spin configurations. An $8 \times 8 \times 2$ Γ -centered k -point mesh was used for the supercell. Symmetry mode analysis was done using AMPLIMODES [27,28].

We begin with unveiling the unstrained bulk ground-state crystal and magnetic structure. First of all, we investigated the most stable spin configuration for the parent $I4/mmm$ structure. As a result, the FM configuration is found to be stable (see Table S2 and Fig. S2 of the Supplemental Material [25]). The total energies of F1 and F2 types are comparable.

Next, we perform stable crystal structure exploration using lattice-dynamics calculations starting from the distortion-free parent $I4/mmm$ structure with a FM spin configuration. Figure 2(a) shows the phonon band structure of the parent $I4/mmm$ phase. There are two unstable phonon modes with imaginary frequencies transforming like irreducible representations (irreps) X_3^- and X_4^- , while there are no unstable modes at the Γ and M points. Both of the two X -point unstable modes are doubly degenerated because the star of the wave vector has another arm [29]. Figures 1(c) and 1(e) illustrate the displacement patterns of $X_3^-(a, a)$ and $X_3^-(a, 0)$ modes, which are characterized by tilting of NiO_6 octahedra along $[1\bar{1}0]$ and $[100]/[010]$ axes, respectively. The displacement patterns of the X_4^- modes are similar to those

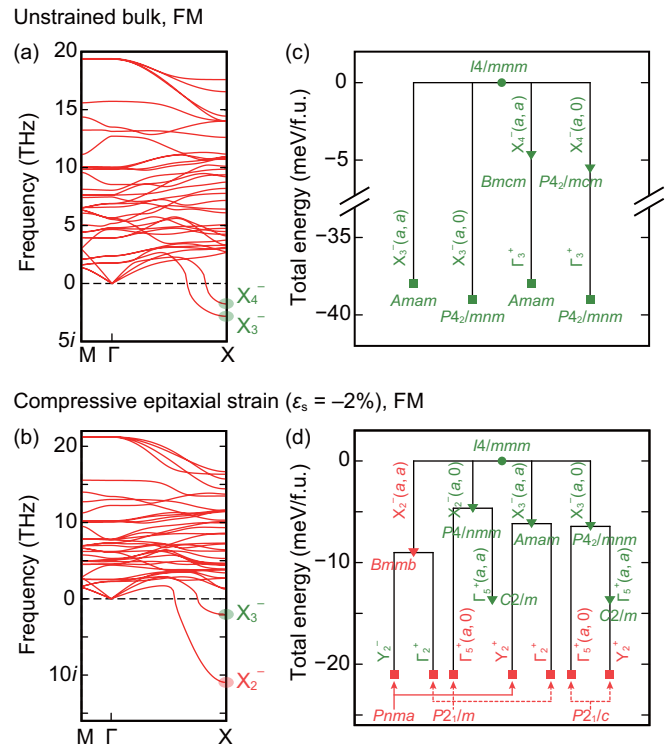


FIG. 2. Phonon band structures between the $M(\frac{1}{2}, \frac{1}{2}, -\frac{1}{2})$, $\Gamma(0,0,0)$, and $X(0, 0, \frac{1}{2})$ points for the parent $I4/mmm$ phase with a FM spin configuration (a) in the unstrained bulk state and (b) under compressive strain ($\epsilon_s = -2\%$). The range of the vertical axes lower than zero has imaginary unit. Treelike line diagrams of $\text{La}_3\text{Ni}_2\text{O}_7$ summarizing the results of the stable-structure search (c) in the unstrained bulk state and (d) under compressive strain ($\epsilon_s = -2\%$). Phases indicated by green and red colors are metallic and insulating, respectively. Circles, squares, and triangles indicate parent, dynamically stable, and unstable phases, respectively. Irreps of unstable phonon modes are also shown.

of the X_3^- modes except a difference in the sense of tilts between adjacent double perovskite blocks. After distorting the parent structure according to these unstable modes, we optimized the lattice constants and atomic coordinates under the symmetry constraint. The $X_3^-(a, a)$, $X_3^-(a, 0)$, $X_4^-(a, a)$, and $X_4^-(a, 0)$ distortions generate $Amam$, $P4_2/mnm$, $Bmcm$, and $P4_2/mcm$ phases, the total energies of which are -38 , -39 , -5 , and -5 meV/f.u., respectively, with regard to that of the parent $I4/mmm$ phase, as shown in Fig. 2(c). Subsequent phonon calculations for the relaxed structures indicate that the $Amam$ and $P4_2/mnm$ phases are dynamically stable, while the $Bmcm$ and $P4_2/mcm$ phases still have unstable phonon modes. Distorting the $Bmcm$ and $P4_2/mcm$ structures according to the unstable modes and optimizing the structural parameters, they are relaxed to the dynamically stable $Amam$ and $P4_2/mnm$ phases, respectively. After the structural exploration, total energies are calculated for all the obtained phases with the eight magnetic configurations. As a result, FM spin configurations are the most stable for all the phases (see Table S2 of the Supplemental Material [25]). Thus, our calculations reveal that either the $Amam$ or $P4_2/mnm$ phase with the FM spin configuration, possessing comparable energies, is

the unstrained bulk ground state of $\text{La}_3\text{Ni}_2\text{O}_7$. It is also found that both the phases are metallic. The *Amam* structure and its metallic behavior have been revealed by previous neutron diffraction [14,30], electrical transport [8–10,14], and theoretical studies [18]. The calculated lattice constants of a , b , and c for the *Amam* phase are 5.36, 5.44, and 20.01 Å, respectively (see Table S7 of the Supplemental Material [25]), which are close to the experimental values; a , b , and c are 5.39, 5.45, and 20.50 Å, respectively [14,30]. Here, it should be noted that the structures characterized by tilting of oxygen octahedra along $[1\bar{1}0]$ and $[100]/[010]$ axes, which correspond to the *Amam* and $P4_2/mnm$ phases for $\text{La}_3\text{Ni}_2\text{O}_7$, are often energetically competing in many other Ruddlesden-Popper phases [31,32]. The $P4_2/mnm$ phase could be an energetically competing metastable phase at room temperature for $\text{La}_3\text{Ni}_2\text{O}_7$. As for the magnetic properties, $\text{La}_3\text{Ni}_2\text{O}_7$ is experimentally reported to be paramagnetic down to low temperatures [8,9,14], which is different from our calculation results. Also for LaNiO_3 , which is one of the most studied materials in the La-Ni-O system, previous LDA + U studies reported that a ferromagnetic state is stable [33], whereas paramagnetic behavior is observed experimentally [34]. These results imply that it is hard to correctly describe magnetic structures of La-Ni-O system by DFT + U calculations because LDA + U hardly describes spin fluctuations near the quantum critical point [35].

Let us move to the exploration of the ground-state structure under epitaxial strain. Here, we define epitaxial strain as $\epsilon_s = (a - a_0)/a_0$, where a is an in-plane lattice constant for $\sqrt{2} \times \sqrt{2} \times 1$ supercells, and $a_0 = 5.37$ Å, which is a theoretical value of the unstrained bulk $I4/mmm$ phase. The stable structure exploration is carried out under $\epsilon_s = \pm 2\%$ in the same manner as in the case of the unstrained bulk condition, starting from the FM $I4/mmm$ phase, except keeping in-plane lattice constants fixed [$a = b = (1 + \epsilon_s)a_0$] even for orthorhombic polymorphs, where a is not necessarily equal to b in terms of symmetry. Figure 2(d) represents the treelike line diagram summarizing the results of the structural exploration at $\epsilon_s = -2\%$. Figure 2(b) shows the phonon band structure of the parent FM $I4/mmm$ phase at $\epsilon_s = -2\%$. Two doubly degenerated unstable phonon modes transforming like irreps X_2^- and X_3^- are obtained. The X_3^- modes bring the parent $I4/mmm$ phase to *Amam* and $P4_2/mnm$ polymorphs, which are dynamically stable under the unstrained condition but are dynamically unstable at $\epsilon_s = -2\%$ (see Fig. S4 of the Supplemental Material [25]). The *Amam* polymorph is distorted by the unstable modes transforming like the irreps Y_2^+ and Γ_2^+ , resulting in *Pnma* and $P2_1/m$ phases, respectively. The $P4_2/mnm$ polymorph transforms to $P2_1/c$ and $C2/m$ phases via unstable $\Gamma_5^+(a, 0)$ and $\Gamma_5^+(a, a)$ modes, respectively. The $C2/m$ phase still has an unstable Y_2^+ mode, resulting in the $P2_1/c$ phase. The three phases *Pnma*, $P2_1/m$, and $P2_1/c$ are found to be dynamically stable and energetically comparable to each other. Their relevant distortions with respect to the $I4/mmm$ phase are represented by a combination of the same irreps $X_2^- \oplus X_3^-$ but with different order parameter directions, as shown in Table I, indicating that these phases are structurally similar to each other. The X_2^- modes are characterized by breathing motion of the NiO_6 octahedra, i.e., alternate stretching and shrinking

TABLE I. Space-group symbols (SG), space-group numbers (SG No.), irreducible representations (irrep) of condensed modes, band gaps (E_g) in units of eV, and total energies (ΔE) in units of meV/f.u. for structures obtained from stable structure exploration under compressive strain ($\epsilon_s = -2\%$) with ferromagnetic (FM) and A2-type antiferromagnetic (AFM) configurations. The total energies are relative to that of the FM $I4/mmm$ phase.

SG (SG No.)	Irrep	FM		AFM	
		E_g	ΔE	E_g	ΔE
<i>Pnma</i> (62)	$X_2^-(a, a) \oplus X_3^-(b, -b)$	0.37	-21	0.64	-55
$P2_1/c$ (14)	$X_2^-(a, a) \oplus X_3^-(b, c)$	0.38	-21	0.63	-55
$P2_1/m$ (11)	$X_2^-(a, a) \oplus X_3^-(b, b)$	0.36	-21	0.61	-55
<i>Bmmb</i> (63)	$X_2^-(a, a)$	0.29	-10	0.61	-39
$C2/m$ (12)	$X_3^-(a, 0) \oplus X_2^-(0, b)$	Metal	-14	Metal	-31
$P4/nmm$ (129)	$X_2^-(a, 0)$	Metal	-4	Metal	-15
$P4_2/mnm$ (136)	$X_3^-(a, 0)$	Metal	-8	Metal	-7
<i>Amam</i> (63)	$X_3^-(a, a)$	Metal	-8	Metal	-6

of the octahedra [Figs. 1(b) and 1(d)]. The $X_2^-(a, a)$ and $X_2^-(a, 0)$ modes are unstable for the parent $I4/mmm$ phase, leading to *Bmmb* and $P4/nmm$ polymorphs, respectively. The *Bmmb* phase has unstable tilting modes transforming like irreps Y_2^- and Γ_2^+ , leading to *Pnma* and $P2_1/m$ polymorphs, respectively, which are the same phases as those obtained through the *Amam* phase. On the other hand, the $P4/nmm$ phase has also unstable tilting modes transforming like irreps $\Gamma_5^+(a, 0)$ and $\Gamma_5^+(a, a)$, leading to the $P2_1/m$ and $C2/m$ polymorphs, respectively. Thus, we found the three dynamically and most stable phases with *Pnma*, $P2_1/m$, and $P2_1/c$ space groups.

All of the obtained polymorphs with the eight magnetic configurations are calculated after the structural search is finished. As a result, the *Pnma*, $P2_1/m$, and $P2_1/c$ phases with the A1- and A2-type AFM configurations are the most stable and energetically comparable to each other. Table I enumerates the structures obtained from the stable structure exploration at $\epsilon_s = -2\%$ and their total energies and band gaps for FM and A2-type AFM configurations. Interestingly, the three dynamically stable phases and the *Bmmb* phase have nonzero electronic band gaps, that is, they are insulating. All the insulating phases involve the $X_2^-(a, a)$ breathing modes, which are softened by the compressive strain. The breathing mode is responsible for the opening of the band gap, as confirmed by the dependence of the band gap on the amplitude of the $X_2^-(a, a)$ mode (see Fig. S7 in the Supplemental Material [25]). On the other hand, the band gaps are closed for the structures involving the $X_2^-(a, 0)$ breathing modes, such as $P4/nmm$ and $C2/m$, where breathing and undistorted double perovskite blocks are stacked alternately [Fig. 1(d)]. The breathing distortion in all the blocks is responsible for the insulating nature. Another interesting thing is that the A1- and A2-type AFM configurations are energetically favored compared to the FM configuration for all the insulating phases. These facts indicate that the compressive strain brings about FM-AFM switching as well as the MI transition through a strong coupling of lattice, charge, and spin degrees of freedom. Hereafter, we focus on the A2-type AFM *Pnma*

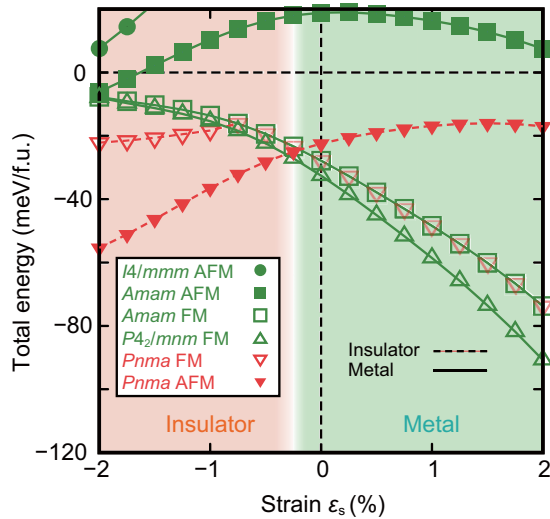


FIG. 3. Total energies of relevant structures as a function of epitaxial strain with respect to that of the FM $I4/mmm$ phase. The energies of structures with FM and A2-type AFM configurations correspond to open and filled symbols, respectively. The white blurred area around $\epsilon_s = -0.3\%$ indicates the phase boundary between the A2-type AFM $Pnma$ and FM $P4_2/mnm$ phases.

phase as the ground-state structure at $\epsilon_s = -2\%$ since $Pnma$, $P2_1/m$, and $P2_1/c$ phases have very similar structures, total energies, and band gaps. The structural parameters are described in Table S8 of the Supplemental Material [25]. It should be noted that the same ground-state phases are derived when the crystal structure exploration starts from the A2-type AFM $I4/mmm$ phase at $\epsilon_s = -2\%$ (see details in the Supplemental Material, Sec. IV [25]). Meanwhile, under 2% tensile strain, a metallic FM $P4_2/mnm$ phase is found to be the most stable (see details in the Supplemental Material, Sec. VI [25]).

Figure 3 plots the total energies of the relevant stable phases as a function of the epitaxial strain with respect to that of the FM $I4/mmm$ phase. The phase boundary between the metallic FM $Amam$ and insulating A2-type AFM $Pnma$ phases lays at $\epsilon_s = -0.3\%$. The moderate critical strain for the MI transition may correspond to the experimental observation that $La_3Ni_2O_7$ is a borderline metal.

A detailed analysis of the electronic band structures allows us to understand the mechanism behind the strain-induced MI transition. Figures 4(a) and 4(b) depict the electronic band structures of the unstrained bulk and compressed ($\epsilon_s = -2\%$) FM $Amam$ phases for majority (up) spin, respectively, between $\Gamma(0,0,0)$ and $Y(\frac{1}{2}, \frac{1}{2}, 0)$ points. As illustrated in the primitive $Amam$ cell shown in Fig. 4(e), the Γ - Y vector ($\frac{1}{2}\mathbf{a}^* + \frac{1}{2}\mathbf{b}^*$) is parallel to the layers. The band structures of both the unstrained bulk and compressed FM $Amam$ phases manifest themselves metallic behavior, irrespective of the presence of strain. A common feature is that band crossing occurs in the proximity of the middle point between Γ and Y , ($\frac{1}{4}, \frac{1}{4}, 0$). One can see a slight difference in the two band structures. The intersection is located slightly below the Fermi level ϵ_F in the unstrained bulk state. On the other hand, 2% compressive strain pushes up the intersection to ϵ_F , tailoring a

situation that maximizes an energy gain by a Peierls transition accompanied by condensation of the lattice mode at Y , which leads to a band folding at $(\frac{1}{4}, \frac{1}{4}, 0)$. Figures 4(c) and 4(d) show the band diagrams of the FM and A2-type AFM $Pnma$ phases at $\epsilon_s = -2\%$, which are derived from the $Amam$ phase by the Y_2^+ distortion. The band diagrams are drawn along the line connecting Γ - $X(\frac{1}{2}, 0, 0)$ - $(1, 0, 0)$, which corresponds to the line between Γ and Y for the $Amam$ phase. One can see band-gap opening at the zone boundary, which stabilizes the electrons near ϵ_F . Figures 4(f) and 4(g) depict the Fermi surface cross section in a plane passing through Γ , Y , and Z , which is parallel to the layer, for the unstrained bulk and $\epsilon_s = -2\%$ FM $Amam$ phase, respectively. One can see that Fermi surface nesting becomes more prominent for the compressively strained state than for the unstrained bulk state, suggesting the stronger Peierls instability under the compressive strain. Thus, we find the subtle change in the band structure by compressive strain to be an origin of the Peierls MI transition. We also confirmed the Fermi surface nesting in the unstrained bulk $I4/mmm$ phase with the A2-type AFM configuration, which shows the instability of breathing phonon modes, but not for that with the FM configuration (see Figure S6 of the Supplemental Material [25]).

Furthermore, the MI transition can also be elucidated from the viewpoint of the effects of octahedral breathing on Ni d orbitals by having a close look at the difference in partial density of state (PDOS) between the metallic and insulating phases. Figure 4(h) shows atom-projected PDOS for the unstrained bulk FM $Amam$ phase. The bands around ϵ_F consist mainly of O $2p$ and Ni $3d$ states, which are strongly interacting with each other. Here, we focus on how partially filled Ni $3d$ states are affected by the breathing distortion. Figure 4(i) shows d - e_g PDOS for the $\epsilon_s = -2\%$ FM $Amam$ phase, which has just one crystallographic Ni site. The bands near ϵ_F are composed of d_{z^2} and $d_{x^2-y^2}$ (e_g) state, while completely filled d_{xy} , d_{yz} , and d_{zx} (t_{2g}) states are lying below -1 eV (not shown), indicating a low-spin configuration. The roughly half-filled $d_{x^2-y^2}$ states are located above the mostly occupied d_{z^2} states; the in-plane Ni-O bonds (1.87 Å) are shorter than the out-of-plane bonds (2.09 Å). Meanwhile, in the FM $Pnma$ phase, the breathing lattice distortion results in two inequivalent crystallographic sites of Ni ions: Ni1 and Ni2 sites. Figures 4(j) and 4(k) depict d - e_g PDOS for Ni ions at the Ni1 and Ni2 sites, respectively. The locations of the two d - e_g states are affected by the deformation of the octahedra due to the breathing mode; in particular, the $d_{x^2-y^2}$ states are strongly influenced because four in-plane Ni-O bonds are involved. Since the Ni1 site is enclosed by a deformed oxygen octahedron with four elongated in-plane Ni-O bonds (1.90 Å) and two compressed out-of-plane Ni-O bonds (2.07 Å), the $d_{x^2-y^2}$ and d_{z^2} states are largely stabilized and a little destabilized, respectively. Thereby, both the d_{z^2} and $d_{x^2-y^2}$ states are fairly occupied. On the other hand, because the Ni2 site is encompassed by an octahedron with four compressed in-plane Ni-O bonds (1.84 Å) and two elongated out-of-plane Ni-O bonds (2.11 Å), the $d_{x^2-y^2}$ states are lifted up significantly while the d_{z^2} states are pushed down slightly, making the $d_{x^2-y^2}$ and d_{z^2} states mostly empty and occupied, respectively. Thus, the breathing lattice distortion causes a charge disproportionation of the Ni d electrons, which leads to the band-gap opening.

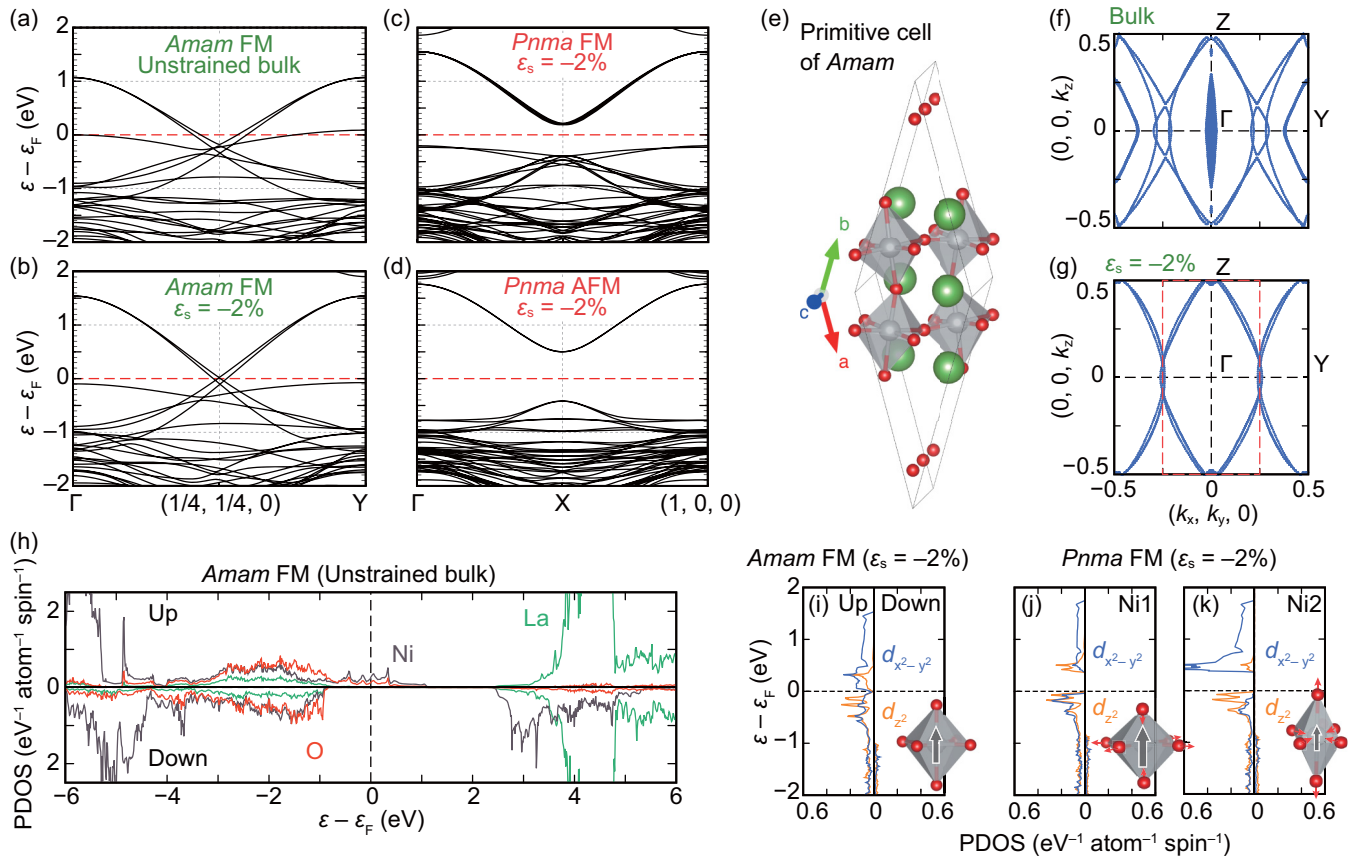


FIG. 4. Electronic band structures of the (a) unstrained bulk and (b) $\epsilon_s = -2\%$ FM *Amam* phases, and the $\epsilon_s = -2\%$ (c) FM and (d) *A2*-type AFM *Pnma* phases. The red broken line indicates Fermi level. The bands are drawn between $\Gamma(0,0,0)$ and $Y(\frac{1}{2}, \frac{1}{2}, 0)$ points for *Amam* and between $\Gamma(0,0,0)$ and $(1,0,0)$ points for *Pnma*. (e) Schematic of a primitive cell for *Amam* structure and directions of lattice vectors. Fermi surfaces of FM *Amam* phase (f) in the unstrained bulk state and (g) under 2% compressive strain when $U_{\text{eff}} = 7$ eV. (h) Atom-projected PDOS of the unstrained bulk FM *Amam*. (i) Orbital-projected PDOS for the d_{-e_g} states of Ni ions in $\epsilon_s = -2\%$ FM *Amam* and that of Ni ions at the (j) Ni1 and (k) Ni2 sites (see text for details) in $\epsilon_s = -2\%$ FM *Pnma*.

We should mention the U_{eff} dependence of the phase stability and band gap (see Sec. VIII of the Supplemental Material [25]). The values of U_{eff} higher than 6.5 eV are required to obtain an experimentally observed metallic *Amam* (or *P4₂/mnm*) phase as an unstrained bulk ground state [14,30]. For this reason, we mainly use $U_{\text{eff}} = 7$ eV, which is comparable to or larger than those used in previous theoretical work for La-Ni-O systems, $U_{\text{eff}} = 4.75$ [18,36,37], 5 [38], and 7 eV [39]. In particular, we have confirmed that the Fermi surface nesting by compressive strain occurs with $U_{\text{eff}} = 3, 5$ eV, but it does not occur with $U_{\text{eff}} = 0, 1.5$ eV (see Figs. S10 and S11 of the Supplemental Material [25]). These results indicate that the MI transition with Peierls mechanism occurs in the wide range of $U_{\text{eff}} (\geq 3$ eV). At $U_{\text{eff}} = 6.5$ eV or lower, the unstrained bulk ground state is the insulating *A2*-type AFM *Pnma* phase. The energetics for the FM *Amam* and *A2*-type AFM *Pnma* phases is attributed to the magnetic interactions, the instability of breathing distortion, and the spin-phonon (lattice) coupling, the U_{eff} dependence of which results in the interesting observation that the ground state is switched from insulating to metallic with an increase in U_{eff} . The band gap of the *A2*-type AFM *Pnma* phase becomes narrower with an increase in U_{eff} above 5.5 eV. This trend is in sharp contrast to Mott-Hubbard and charge-transfer insulators, for

which higher U_{eff} values lead to larger band gaps. One can see clear correlation between the band gap and the amplitude of the breathing mode as a function of U_{eff} (see Fig. S8(b) of the Supplemental Material [25]). On the other hand, at $U_{\text{eff}} = 1$ eV and lower, the unstrained bulk *A2*-type AFM *Pnma* is relaxed into a nonmagnetic metallic *Amam* phase. The insulating states are not stabilized in this small- U_{eff} regime as in Mott-Hubbard type or charge-transfer insulators. Both the onsite Coulomb repulsion and the breathing distortion are necessary for the band-gap opening in this material.

Lastly, we compare the mechanisms behind MI transitions in various nickelate perovskite derivatives for systematic understanding. In rare-earth nickelate simple perovskites, temperature-induced MI transitions are observed. As the ionic radius of the rare earth is decreased, the MI transition temperature becomes higher [40–43]. The MI transition is concomitant with a structural transition from orthorhombic *Pnma* to monoclinic *P2₁/c* phases, which involves a breathing distortion of the NiO₆ octahedra and hence a disproportionation of the Ni sites, Ni-O bonds, and charges [42]. But, key factors for the MI transition and structural transition are not completely understood yet, although it has been intensely debated; both local correlation effects such as onsite Coulomb repulsion and Hund coupling [44] and band-structure effects such as

charge fluctuation [45] and Peierls transition [46] have been proposed as the key factors. Recently, the mechanism of the dramatic increase in resistivity of an oxygen-deficient triple-layered Ruddlesden-Popper phase $\text{La}_4\text{Ni}_3\text{O}_8$ at 105 K has been identified as charge ordering of Ni ions by synchrotron x-ray diffraction [47] and first-principles calculations [36]. A combination of buckling distortion of the NiO_2 planes and antiferromagnetic ordering results in the insulating charge-ordered state ($3\text{Ni}^{1.33+} \rightarrow 2\text{Ni}^+ + \text{Ni}^{2+}$) [36]. In this study, we revealed that in $\text{La}_3\text{Ni}_2\text{O}_7$, as in the compounds mentioned above, the MI transition is accompanied by subtle lattice distortions; the octahedral breathing modes generate inequivalent Ni sites and hence lead to charge disproportionation, resulting in the insulating state. Our calculations show that both the local electronic correlation effect such as $U_{\text{eff}} = 3, 5, \text{ and } 7$ eV and band-structure effect such as the Fermi surface nesting are key factors for the MI transition.

In conclusion, we have investigated the epitaxial-strain dependence of crystal, electronic, and magnetic ground-state phase stability of $\text{La}_3\text{Ni}_2\text{O}_7$ from first principles. We found that while unstrained bulk $\text{La}_3\text{Ni}_2\text{O}_7$ is metallic and FM, moderate compressive strain drives it to an insulating and AFM phase, demonstrating a strong coupling of spin, charge,

and lattice degrees of freedom. The subtle modification of the electronic band structure by compressive strain enhances a Peierls instability, leading to the NiO_6 octahedral breathing distortion. The band-gap opening microscopically originates from the opposite $3d-e_g$ level shifts of the inequivalent Ni ions generated by the breathing distortion. Our study thus shows that the lanthanum nickelate is a possible platform where the electric conductivity can be tuned by external fields such as strain via a strong lattice-charge-spin coupling.

The authors thank Dr. Yuichiro Matsushita for the discussion. This work was supported by Japan Society for the Promotion of Science (JSPS) KAKENHI Grants No. JP18J21747, No. JP16H06793, No. JP17K19172, and No. JP18H01892, Elements Strategy Initiative to Form Core Research Center and Creation of Life Innovation Materials for Interdisciplinary and International Researcher Development project from Ministry of Education, Culture, Sports, Science and Technology, Support Program for Starting Up Innovation Hub MI²I from Japan Science and Technology Agency (JST), and Murata Science Foundation. The visualization of crystal structures in Figs. 1(a), 4(e), and 4(i)–4(k) was done by VESTA [48], which is acknowledged.

-
- [1] D. G. Schlom, L.-Q. Chen, C. J. Fennie, V. Gopalan, D. A. Muller, X. Pan, R. Ramesh, and R. Uecker, *MRS Bull.* **39**, 118 (2014).
- [2] J. Wang, J. B. Neaton, H. Zheng, V. Nagarajan, S. B. Ogale, B. Liu, D. Viehland, V. Vaithyanathan, D. G. Schlom, U. V. Waghmare *et al.*, *Science* **299**, 1719 (2003).
- [3] J. H. Haeni, P. Irvin, W. Chang, R. Uecker, P. Reiche, Y. L. Li, S. Choudhury, W. Tian, M. E. Hawley, B. Craigo *et al.*, *Nature (London)* **430**, 758 (2004).
- [4] J. H. Lee, L. Fang, E. Vlahos, X. Ke, Y. W. Jung, L. F. Kourkoutis, J.-W. Kim, P. J. Ryan, T. Heeg, M. Roeckerath *et al.*, *Nature (London)* **466**, 954 (2010).
- [5] A. K. Yadav, C. T. Nelson, S. L. Hsu, Z. Hong, J. D. Clarkson, C. M. Schlepütz, A. R. Damodaran, P. Shafer, E. Arenholz, L. R. Dedon *et al.*, *Nature (London)* **530**, 198 (2016).
- [6] J. M. Rondinelli, S. J. May, and J. W. Freeland, *MRS Bull.* **37**, 261 (2012).
- [7] F. Gervais, P. Odier, and Y. Nigara, *Solid State Commun.* **56**, 371 (1985).
- [8] R. Ram, L. Ganapathi, P. Ganguly, and C. Rao, *J. Solid State Chem.* **63**, 139 (1986).
- [9] Z. Zhang, M. Greenblatt, and J. Goodenough, *J. Solid State Chem.* **108**, 402 (1994).
- [10] S. Taniguchi, T. Nishikawa, Y. Yasui, Y. Kobayashi, J. Takeda, S. ichi Shamoto, and M. Sato, *J. Phys. Soc. Jpn.* **64**, 1644 (1995).
- [11] Y. Kobayashi, S. Taniguchi, M. Kasai, M. Sato, T. Nishioka, and M. Kontani, *J. Phys. Soc. Jpn.* **65**, 3978 (1996).
- [12] D.-K. Seo, W. Liang, M.-H. Whangbo, Z. Zhang, and M. Greenblatt, *Inorg. Chem.* **35**, 6396 (1996).
- [13] M. Greenblatt, Z. Zhang, and M. Whangbo, *Synth. Met.* **85**, 1451 (1997).
- [14] C. D. Ling, D. N. Argyriou, G. Wu, and J. Neumeier, *J. Solid State Chem.* **152**, 517 (2000).
- [15] G. Wu, J. J. Neumeier, and M. F. Hundley, *Phys. Rev. B* **63**, 245120 (2001).
- [16] V. V. Poltavets, K. A. Lokshin, T. Egami, and M. Greenblatt, *Mater. Res. Bull.* **41**, 955 (2006).
- [17] T. Hosoya, K. Igawa, Y. Takeuchi, K. Yoshida, T. Uryu, H. Hirabayashi, and H. Takahashi, *J. Phys.: Conf. Ser.* **121**, 052013 (2008).
- [18] V. Pardo and W. E. Pickett, *Phys. Rev. B* **83**, 245128 (2011).
- [19] J. H. Lee, G. Luo, I. C. Tung, S. H. Chang, Z. Luo, M. Malshe, M. Gadre, A. Bhattacharya, S. M. Nakhmanson, J. A. Eastman *et al.*, *Nat. Mater.* **13**, 879 (2014).
- [20] P. E. Blöchl, *Phys. Rev. B* **50**, 17953 (1994).
- [21] J. P. Perdew, A. Ruzsinszky, G. I. Csonka, O. A. Vydrov, G. E. Scuseria, L. A. Constantin, X. Zhou, and K. Burke, *Phys. Rev. Lett.* **100**, 136406 (2008).
- [22] G. Kresse and J. Furthmüller, *Phys. Rev. B* **54**, 11169 (1996).
- [23] G. Kresse and D. Joubert, *Phys. Rev. B* **59**, 1758 (1999).
- [24] S. L. Dudarev, G. A. Botton, S. Y. Savrasov, C. J. Humphreys, and A. P. Sutton, *Phys. Rev. B* **57**, 1505 (1998).
- [25] See Supplemental Material at <http://link.aps.org/supplemental/10.1103/PhysRevMaterials.2.125001> for the details of schematics of eight magnetic structures, phonon band structure of AFM $I4/mmm$ and FM $Amam$, the results of stable structure exploration under tensile strain, and the U_{eff} dependence of MI phase boundary.
- [26] A. Togo and I. Tanaka, *Scr. Mater.* **108**, 1 (2015).
- [27] D. Orobengoa, C. Capillas, M. I. Aroyo, and J. M. Perez-Mato, *J. Appl. Crystallogr.* **42**, 820 (2009).
- [28] J. M. Perez-Mato, D. Orobengoa, and M. I. Aroyo, *Acta Crystallogr., Sect. A* **66**, 558 (2010).
- [29] There are two X points $(0,0,\frac{1}{2})$ and $(-\frac{1}{2},\frac{1}{2},0)$ for the primitive cell of $I4/mmm$ structure, indicating that the Γ -X vector has two arms, which are perpendicular to each other. As in the case

- of conventional cell, the two X points are represented as $(\frac{1}{2}, \frac{1}{2}, 0)$ and $(\frac{1}{2}, -\frac{1}{2}, 0)$.
- [30] V. I. Voronin, I. F. Berger, V. A. Cherepanov, L. Y. Gavrilova, A. N. Petrov, A. I. Ancharov, B. P. Tolochko, and S. G. Nikitenko, *Nucl. Instrum. Methods Phys. Res., Sect. A* **470**, 202 (2001).
- [31] M. J. Pitcher, P. Mandal, M. S. Dyer, J. Alaria, P. Borisov, H. Niu, J. B. Claridge, and M. J. Rosseinsky, *Science* **347**, 420 (2015).
- [32] H. Akamatsu, K. Fujita, T. Kuge, A. Sen Gupta, A. Togo, S. Lei, F. Xue, G. Stone, J. M. Rondinelli, L.-Q. Chen, I. Tanaka, V. Gopalan, and K. Tanaka, *Phys. Rev. Lett.* **112**, 187602 (2014).
- [33] G. Gou, I. Grinberg, A. M. Rappe, and J. M. Rondinelli, *Phys. Rev. B* **84**, 144101 (2011).
- [34] K. Sreedhar, J. M. Honig, M. Darwin, M. McElfresh, P. M. Shand, J. Xu, B. C. Crooker, and J. Spalek, *Phys. Rev. B* **46**, 6382 (1992).
- [35] A. G. Petukhov, I. I. Mazin, L. Chioncel, and A. I. Lichtenstein, *Phys. Rev. B* **67**, 153106 (2003).
- [36] A. S. Botana, V. Pardo, W. E. Pickett, and M. R. Norman, *Phys. Rev. B* **94**, 081105 (2016).
- [37] V. Pardo and W. E. Pickett, *Phys. Rev. Lett.* **105**, 266402 (2010).
- [38] T. Liu, H. Wu, T. Jia, X. Zhang, Z. Zeng, H. Q. Lin, and X. G. Li, *AIP Adv.* **4**, 047132 (2014).
- [39] V. V. Poltavets, M. Greenblatt, G. H. Fecher, and C. Felser, *Phys. Rev. Lett.* **102**, 046405 (2009).
- [40] J. B. Torrance, P. Lacorre, A. I. Nazzal, E. J. Ansaldo, and C. Niedermayer, *Phys. Rev. B* **45**, 8209 (1992).
- [41] J. L. García-Muñoz, J. Rodríguez-Carvajal, P. Lacorre, and J. B. Torrance, *Phys. Rev. B* **46**, 4414 (1992).
- [42] J. A. Alonso, J. L. García-Muñoz, M. T. Fernández-Díaz, M. A. G. Aranda, M. J. Martínez-Lope, and M. T. Casais, *Phys. Rev. Lett.* **82**, 3871 (1999).
- [43] S. Middey, J. Chakhalian, P. Mahadevan, J. Freeland, A. Millis, and D. Sarma, *Annu. Rev. Mater. Res.* **46**, 305 (2016).
- [44] A. Subedi, O. E. Peil, and A. Georges, *Phys. Rev. B* **91**, 075128 (2015).
- [45] Y. Lu, Z. Zhong, M. W. Haverkort, and P. Hansmann, *Phys. Rev. B* **95**, 195117 (2017).
- [46] A. Mercy, J. Bieder, J. Iniguez, and P. Ghosez, *Nat. Commun.* **8**, 1677 (2017).
- [47] J. Zhang, Y.-S. Chen, D. Phelan, H. Zheng, M. R. Norman, and J. F. Mitchell, *Proc. Natl. Acad. Sci. USA* **113**, 8945 (2016).
- [48] K. Momma and F. Izumi, *J. Appl. Crystallogr.* **44**, 1272 (2011).